Moesin orchestrates cortical polarity of melanoma tumour cells to initiate 3D invasion

Ana Estecha[1], Lorena Sánchez-Martín[1], Amaya Puig-Kröger[1], Rubén A. Bartolomé[2], Joaquín Teixidó[2], Rafael Samaniego[3,*] and Paloma Sánchez-Mateos[1,3,*,‡]

[1]Laboratorio de Inmuno-oncología and [3]Unidad de Microscopía Confocal, Hospital General Universitario Gregorio Marañón, 28007 Madrid, Spain
[2]Department of Cellular and Molecular Physiopathology, Centro de Investigaciones Biológicas, 28040 Madrid, Spain
*These authors contributed equally to this work
‡Author for correspondence (rsanchezma.hgugm@salud.madrid.org)

Accepted 14 July 2009
Journal of Cell Science 122, 3492-3501 Published by The Company of Biologists 2009
doi:10.1242/jcs.053157

Summary

Tumour cell dissemination through corporal fluids (blood, lymph and body cavity fluids) is a distinctive feature of the metastatic process. Tumour cell transition from fluid to adhesive conditions involves an early polarization event and major rearrangements of the submembrane cytoskeleton that remain poorly understood. As regulation of cortical actin-membrane binding might be important in this process, we investigated the role of ezrin and moesin, which are key crosslinking proteins of the ERM (ezrin, radixin, moesin) family. We used short interfering RNA (siRNA) to show that moesin is crucial for invasion by melanoma cells in 3D matrices and in early lung colonization. Using live imaging, we show that following initial adhesion to the endothelium or 3D matrices, moesin is redistributed away from the region of adhesion, thereby generating a polarized cortex: a stable cortical actin dome enriched in moesin and an invasive membrane domain full of blebs. Using Lifeact-GFP, a 17-amino-acid peptide that binds F-actin, we show the initial symmetry breaking of cortical actin cytoskeleton during early attachment of round cells. We also demonstrated that ezrin and moesin are differentially distributed during initial invasion of 3D matrices, and, specifically, that moesin controls adhesion-dependent activation of Rho and subsequent myosin II contractility. Our results reveal that polarized moesin plays a role in orienting Rho activation, myosin II contractility, and cortical actin stability, which is crucial for driving directional vertical migration instead of superficial spreading on the fluid-to-solid tissue interface. We propose that this mechanism of cortical polarization could sustain extravasation of fluid-borne tumour cells during the process of metastasis.

Supplementary material available online at
http://jcs.biologists.org/cgi/content/full/122/19/3492/DC1

Key words: Invasion, Metastasis, Moesin, Polarity

Introduction

Professional circulating cells such as leukocytes use blood vessels or the lymph system to reach distant tissues. Dissemination through body fluids (blood, lymph, peritoneal or pleural effusions) also plays a major role under pathological conditions, such as cell metastasis or pathogen invasion (Chambers et al., 2002; Sahai, 2007). Circulating cells adopt a symmetric round morphology (the geometrical shape that best resists mechanical stress) and exhibit a thick and rigid skeleton underneath the plasma membrane. The composition of this cortical cytoskeleton, which is rich in actin, actin-bundling proteins and myosin II, is similar to the contractile cortex of other non-adherent cells, such as oocytes, eggs or embryos (Bornens et al., 1989; Rodriguez et al., 2003).

When entering mitosis, cells start to round up upon reorganization of the cortical actomyosin network. Two recent studies have found that phosphorylation of moesin, the only member of the ezrin-radixin-moesin (ERM) protein family in *Drosophila*, plays a key role in shaping the round cortex of mitotic cells (Carreno et al., 2008; Kunda et al., 2008). ERM proteins provide regulated linkage between the plasma membrane and the actin network and are key in the control of cell-surface morphology (Bretscher et al., 2002). Conformational regulation of ERM function occurs by intramolecular and intermolecular association of the N-terminal (FERM; 4.1 protein, ezrin, radixin, moesin) and C-terminal domains, whereby actin-binding activity is masked. Activation of ERM occurs in two steps (Fievet et al., 2004; Niggli and Rossy, 2008): first, ERM molecules target the cell membrane by binding phosphatidylinositol (4,5)-bisphosphate (PtdIns(4,5)P_2) through their FERM domains (Matsui et al., 1999; Niggli et al., 1995; Yonemura et al., 2002); subsequently, phosphorylation at a C-terminal threonine (T567 ezrin, T564 radixin and T558 moesin) stabilizes an open conformation and regulates binding to actin (Matsui et al., 1998). Several gene-profiling studies have identified high expression of ERM proteins associated with the metastatic abilities of cancer cells: ezrin has been shown to play a crucial role in the metastasis of two pediatric sarcomas (Khanna et al., 2004; Yu et al., 2004), and moesin is strongly upregulated in metastatic breast cancer cells collected in vivo and is misregulated in cancers with a poor prognosis (Charafe-Jauffret et al., 2007; Condeelis et al., 2005; Kobayashi et al., 2004).

Metastasis is a multi-step process involving cancer cell motility, intravasation, fluid transportation to a distant organ, extravasation, and growth at the new site (Sahai, 2007). Metastatic cells might need to adopt a rounded shape to efficiently intravasate and survive the hemodynamic rigors of circulation. By contrast, binding to vascular endothelium and extravasation might require a global reorganization of the cytoskeleton into a configuration that is appropriate for a flexible migration-capable cell. Interestingly, rapid conversion of ERMs from their active to inactive conformations has been reported in lymphocytes in response to chemokines, and involves reduction of PtdIns(4,5)P_2 levels by activation of phospholipase C (Brown et al., 2003; Hao et al., 2009). In the current

study, we identified moesin as the ERM protein involved in lung colonization by melanoma cells. Then, we live-imaged the reorganization of moesin and cortical actin away of the region of adhesion to endothelial cells or to collagen. We thoroughly analyzed the phenotype of moesin mutants and moesin-depleted cells following initial attachment.

Results

Moesin is necessary for lung colonization by melanoma cells

To investigate the role of ERM proteins in tumour progression, we used the highly invasive human cell lines BLM, MV3, Skmel-19, Skmel-103, Skmel-147, and the less invasive A375 and MeWo cells for comparison (see below). Immunoblot analyses showed that all invasive cell lines tested expressed considerably more moesin than ezrin or radixin, however BLM cells also expressed a significant amount of ezrin (erzin/moesin ratio 0.53±0.15) (Fig. 1A; supplementary material Fig. S1A). Because there is emerging evidence that each member of the ERM family contributes to both distinct and overlapping cellular functions (Ilani et al., 2007), we used short interfering RNAs (siRNAs) that were specific for moesin or ezrin to study their individual roles. A significant reduction in moesin or ezrin expression was achieved with the corresponding siRNA in BLM, MV3, and Skmel-103 cells without affecting cell viability (Fig. 1A; supplementary material Fig. S1B; and data not shown).

To determine whether ezrin or moesin could influence the ability of melanoma cells to colonize tissues in vivo, we used an assay that compares different siRNA-transfected cells injected into the tail vein of mice. A feature of this short-term assay is that it permits evaluation of specific steps in the metastatic cascade (survival within circulation, and cytoskeletal events important for attachment to blood vessels and extravasation) (Pinner and Sahai, 2008; Tsuji et al., 2006). We chose BLM cells because they had proven to be very efficient in long-term experimental metastasis assays (Van Muijen et al., 1991). Equal numbers of control and moesin or ezrin siRNA transfectants marked with different fluorescent probes were mixed and injected into the tail vein. After 20 minutes, equivalent numbers of each cell type reached the lungs (Fig. 1B). Interestingly, 20 hours after injection, most moesin-depleted cells had disappeared from the lungs, whereas a significant fraction of control cells were clearly detected within the lung parenchyma, out of large vessels (supplementary material Fig. S1C). By contrast, no difference in the number of control and ezrin-depleted cells was observed at any time (Fig. 1B). These results show that BLM melanoma cells require moesin, but not ezrin, for early lung colonization.

Role of moesin and ezrin in 3D collagen invasion

Because metastatic colonization involves active cell attachment and motility, and ERM proteins play a major role in regulating cytoskeletal events (Brown et al., 2003; Faure et al., 2004), we explored the role of ERM proteins in melanoma cell invasion of 3D collagen I matrices. Moesin silencing markedly reduced the number of invasive cells and the depth of invasion in BLM, MV3 and Skmel-103 melanoma cells, compared to control siRNA cells. By contrast, BLM cells were more invasive as ezrin became depleted, whereas Skmel-103 and MV3, which expressed low levels of ezrin, were unaffected by its knockdown (Fig. 2A; supplementary material Fig. S1D). We observed that BLM, MV3 and Skmel-103 cells all displayed elongated morphologies within 3D collagen, typical of the mesenchymal mode of invasion. Notably, in addition to reducing BLM invasion (Fig. 2A), silencing moesin expression caused a change in cell morphology, which appeared flattened on the surface of 3D collagen (Fig. 2B). By contrast, ezrin depletion resulted in a faster acquisition of elongated phenotypes; cells displayed fewer protrusions and were longer than control siRNA cells (48±3 μm versus 39±3 μm, n=30 cells; P<0.03, Student's t-test) (Fig. 2B). Similarly to control BLM cells, invasion of ezrin-depleted cells was dependent on β1 integrins and Rho-ROCK signalling because it was inhibited by a blocking anti-β1 mAb and by Y-27632 (supplementary material Fig. S1E,F). Treatment with the metalloproteinase inhibitor GM6001 did not affect control BLM cell invasion, which was associated with a switch to a more rounded morphology. In addition, both ezrin- and moesin-silenced cells exhibited an enhanced migratory response to 2D collagen compared to control cells, without affecting cell adhesion, indicating that moesin depletion selectively reduced 3D matrix invasion (Fig. 2C). Therefore, moesin and ezrin could play distinct roles in the ability of BLM cells to invade 3D collagen matrices.

Dynamic distribution of moesin during transendothelial invasion

We focused our interest in elucidating the role of moesin in invasion because moesin knockdown consistently inhibited both the entry of tumour cells into 3D matrices and lung colonization. We used a

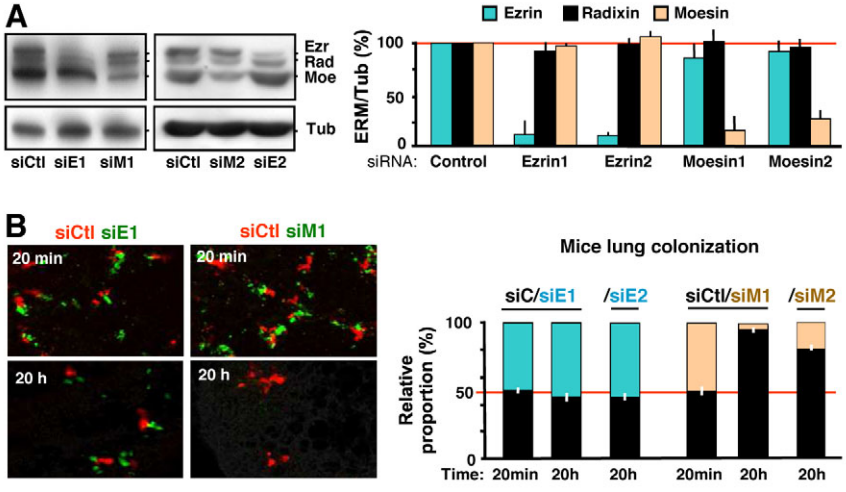

Fig. 1. Moesin downregulation inhibits in vivo lung colonization of melanoma tumour cells. (A) Silencing efficiency of control (siCtl), moesin (siM1 and siM2), and ezrin (siE1 and siE2) siRNAs in BLM cells. Representative immunoblots show ERM proteins, and α-tubulin (Tub) as loading control. Histograms denote the average levels ± s.e. of moesin, ezrin or radixin assessed from two to five independent transfections relative to control (set at 100%). (B) Effects of ezrin and moesin downregulation on mouse lung colonization assays (see Materials and Methods). BLM cells transfected with control siRNAs (red), and with either ezrin1 or moesin1 siRNAs (both in green) were mixed in equal proportions, and injected into the tail vein of mice. Representative confocal sections of lungs extracted 20 minutes and 20 hours after injection are shown. Histograms denote the relative proportion ± s.e. of cells at these times (n=3 mice by time-point and condition). Results obtained with a second pair of siRNAs (siE2 and siM2) are shown at 20 hours post-injection (n=2 mice).

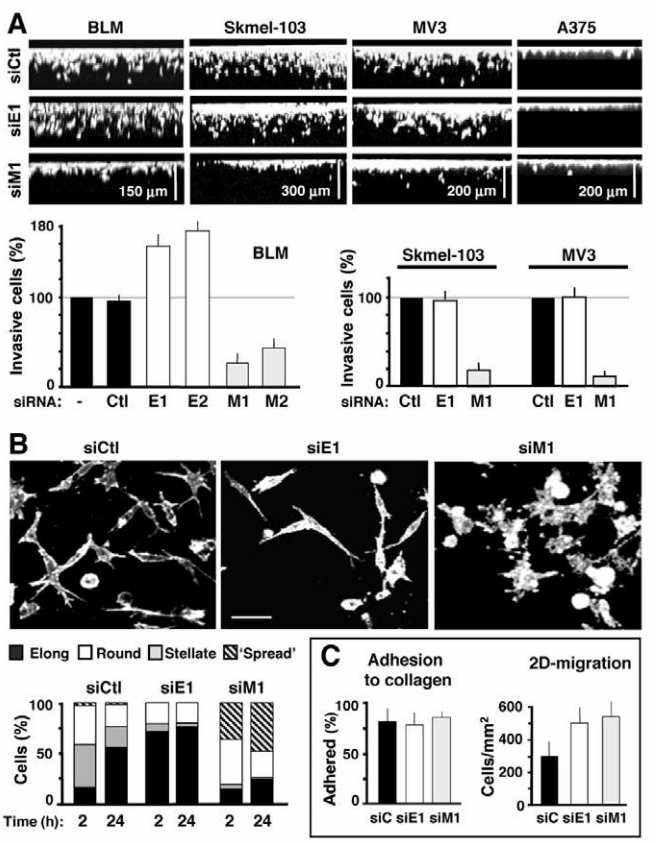

Fig. 2. Moesin downregulation inhibits 3D collagen invasion. (A) Effects of ezrin and moesin downregulation on 3D collagen invasion. Different cell lines were added on top of collagen gels (~300 µm) and allowed to invade for 24 hours (BLM) or 48 hours (Skmel-103, MV3 or A375), as indicated. Images correspond to lateral views (*y*-axis projections of *z*-series) of collagen gels, and the vertical scale-bars indicate matrix depth. Bottom left histogram shows BLM cells transfected with control (Ctl), ezrin (E1 and E2), or moesin (M1 and M2) siRNAs analyzed after 24 hours of invasion. Mean percentages ± s.e. of invasive cells relative to untransfected control cells (set at 100%) are shown (mean of six independent experiments; >1500 invasive cells by siRNA). Right histogram shows Skmel-103 and MV3 cells transfected with control, ezrin or moesin siRNAs after 48 hours of invasion (mean of four independent experiments: >2000 invasive cells by siRNA). Cells were considered invasive beyond 20 µm in depth. (B) Morphological analysis of BLM cells transfected with control (siCtl), moesin1 (siM1) or ezrin1 (siE1) siRNAs invading 3D collagen matrices prepared in multi-well slides. Images correspond to top views (*z*-axis projections of *z*-series) of phalloidin-stained cells after 24 hours of invasion. Scale bar: 30 µm. Histograms denote the relative proportion of distinctive morphologies at 2 hours and 24 hours of invasion (300 cells per experiment, *n*=3): rounded, elongated, stellate (cells with three or more protrusions in different directions), and 'spread' (cells flattened on the gel surface). (C) Comparative analyses of BLM cells transfected with control (siC), moesin1 (siM1), or ezrin1 (siE1) siRNAs. Left: adhesion assay on 2D collagen performed at 10 minutes, as previously described (Longo et al., 2001). Right: migration assay achieved through 8-µm pore membrane Transwells. 10^4 cells were plated on the upper side of the membrane and allowed to migrate for 24 hours towards the lower face (coated with collagen). Cells on the lower side were counted. Histograms represent the mean number ± s.e. of 2D migrated cells per mm^2.

3D model consisting of endothelial cells grown on 3D collagen matrices to study the dynamic distribution of moesin during transendothelial migration of tumour cells (Longo et al., 2001). Tumour cells were added on top of the endothelial surface, and transmigration was followed by confocal microscopy or by silver staining of co-cultures to control monolayer integrity (supplementary material Fig. S2A; Movie 1). To live-image vertical displacements of cells during transmigration, we periodically acquired *z*-series to generate lateral views of invasive cells (Fig. 3A). Typically, ~40% of BLM cells completed transmigration after 24 hours, acquiring more elongated and complex morphologies within the subendothelial matrix. Control cells and cells expressing moesin conjugated to green fluorescent protein (moesin-GFP) remained quite round upon attachment to the endothelium and during transendothelial passage. Moesin-GFP was cortically distributed all around suspended cells, and evenly detected at the tumour-endothelial surface immediately after contact (Fig. 3B, single *xy* section at time 0). Notably, following initial adhesion to the endothelium, moesin-GFP was redistributed away from the region of adhesion towards the unattached dorsal cortex of virtually all transmigrating cells (Fig. 3B; 1-3 minutes single *xy* sections at the level of adhesion, 4 and 45 minutes *xz* lateral views, 22 of 22 live-imaged cells).

To determine whether an endothelial signal was required to induce this pattern of moesin redistribution, cells were plated directly on 3D collagen. These cells also displayed dorsal polarization of moesin-GFP, but not of ezrin conjugated to yellow fluorescent protein (ezrin-YFP), and the same pattern of distribution was observed for the endogenous proteins stained with specific antibodies (Fig. 3C,D; see *xy* sections corresponding to the ventral surface). A polarized moesin distribution at the cell rear was also detected during subsequent invasion, whereas ezrin remained unpolarized (Fig. 3D, endogenous proteins; supplementary material Fig. S2B, moesin-GFP live-imaged during deep invasion).

Interestingly, at the start of 3D matrix invasion, cells consistently exhibited a broken cortical actin appearance with multiple blebs at the invasive pole, whereas cortical actin remained continuous at the dorsal surface (Fig. 3E). Thus, moesin is polarized during the initial attachment of round cells to endothelium or 3D collagen. In addition, two functionally distinct cortical domains take shape: a stable cortical actin dome enriched in moesin and an invasive membrane domain full of blebs.

Moesin distribution during initial attachment and spreading

We observed that moesin polarization also occurred within the initial phases of cell spreading on 2D collagen-coated surfaces (Fig. 4A,B). We standardized our data according to the following spreading phases (Giannone et al., 2004): transition from round to hemispheric cells that display blebs at the periphery of the cell (phase 1 or early spreading), rapid extension of lamellae and flattening of the cell body (phase 2 or intermediate spreading), and a final spread phase when focal adhesions start to form (phase 3, not addressed in this work) (Fig. 5B; see also spreading and invasion models shown later). In all initially spreading cells (phase 1), moesin-GFP displayed a rapid and continuous 'opening' at the attached pole, until a maximum hole diameter was reached in hemispheric cells (10.5±1.6 µm, *n*=30 cells). During intermediate spreading (phase 2), the rim of moesin-GFP completely disappeared from the ventral surface and accumulated in a large apical cap (Fig. 4A).

Interestingly, we used Lifeact-GFP (a 17-amino-acid peptide that binds F-actin) to in vivo visualize actin dynamics (Riedl et al., 2008). We confirmed that Lifeact-GFP colocalized with F-actin stained with phalloidin (supplementary material Fig. S2C), and its distribution was consistent with previous works showing that at early times of spreading there are no stress fibres or focal adhesions and that F-actin forms a scaffold between filopodia at the cell periphery (Partridge and Marcantonio, 2006). Strikingly, Lifeact-GFP

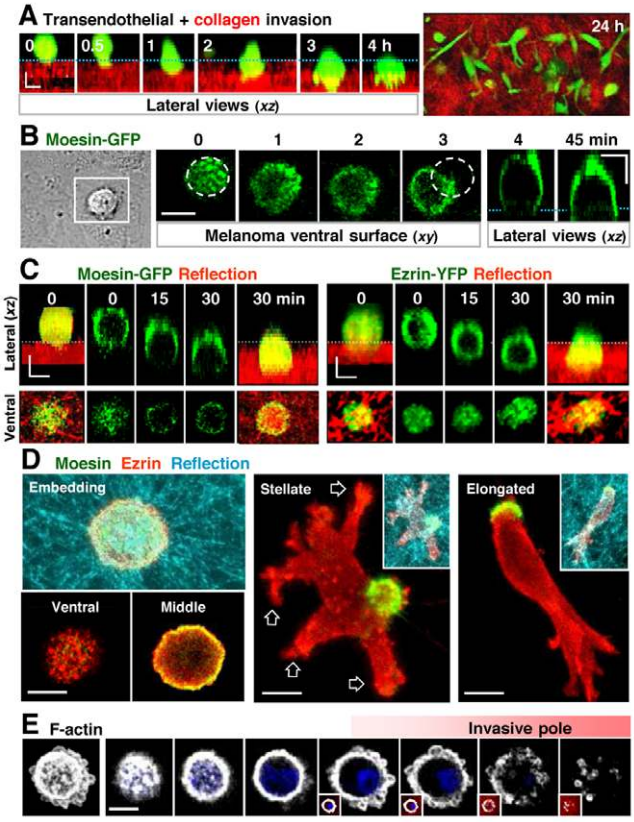

Fig. 3. Dynamic distribution of ezrin and moesin in melanoma cells during endothelial and/or 3D collagen invasion. (A) BLM cells live-imaged during transendothelial- and subendothelial-matrix invasion (see Materials and Methods). BLM cells (green) were added on top of an endothelial monolayer grown on a collagen gel. Images correspond to lateral views of time-lapse *z*-series (*xz* vertical sections were obtained by combining a series of *xy* scans taken along the *z*-axis with the software). The cell first inserts among HUVEC cells (0.5-2 hours), and then initiates subendothelial-matrix invasion (collagen fibres detected with reflected light are in red). The line indicates the position of the endothelial monolayer. Note that invasive cells appear to remodel the collagen fibres under and around the cell, but the collagen surface in areas devoid of melanoma cells remained in the same *z*-plane (see extended panel at 2 hours). The right image is a single confocal *xy* plane 35 µm under the endothelium after 24 hours of invasion. (B) Cell expressing moesin-GFP (green) live-imaged on endothelium (DIC image). Moesin-GFP was imaged at the tumour-endothelial contact surface for 3 minutes (single *xy* basal planes at 0, 1, 2 and 3 minutes are shown), then, *z*-series were acquired at 4 and 45 minutes to generate lateral views (*xz* vertical sections). The initial tumour-cell position at 0 minutes is encircled at 3 minutes, to show the lateral movement of the tumour cell on the endothelial surface. The endothelial monolayer was grown on a thin collagen gel (see Materials and Methods). (C) Cells expressing moesin-GFP (left) and ezrin-YFP (right) (both in green) live-imaged during 3D collagen embedding. Periodic *z*-series were acquired at indicated times; the corresponding lateral views (*xz* vertical sections, top panels) and the basal cell surface (single *xy* planes, bottom panels) are shown. Note that at 30 minutes the lower *z*-limits were enlarged to include deeper collagen. Images showing merged collagen (0 and 30 minutes, in red) are lateral *y*-axis projections. (D) Redistribution of endogenous moesin (green) and ezrin (red) during the initial steps of 3D collagen invasion. The three morphological patterns quantified in Fig. 2B are shown: rounded-embedding (left), stellate (centre, multiple protrusions pointed by arrows) and elongated (right). All images correspond to *z*-projections, except the single *xy* sections taken at the middle and ventral melanoma surface of the embedding cell (left, as indicated). Merged images with collagen fibres are also shown (cyan). (E) BLM cell embedding in 3D collagen stained with phalloidin (white) and DAPI (blue). The top view (left, *z*-projection) and a gallery of single *xy* sections taken at 2 µm intervals, from the apical to the invasive-blebbing pole, are shown. Collagen fibres are in red to position the cell relative to 3D collagen (insets). Scale bars: 10 µm.

displayed the same 'opening' dynamics at the ventral surface as moesin during initial attachment, but remained at the edge of the cell during intermediate spreading (Fig. 4C; 5 and 15 minutes, respectively).

We also compared the distribution of endogenous moesin with cortical actin, which colocalized with myosin II in suspended cells (referred to as the actomyosin contractile cortex). Immunofluorescence staining of round cells adhering to 2D collagen for short times showed a distinctive pattern of contractile cortex disassembly restricted to the adhesive pole (phase 1, hemispheric blebbing cells) (Fig. 4D). During phase 2, moesin and F-actin were increasingly concentrated in the apical cap, whereas myosin II was less accumulated (Fig. 4D, see pseudocoloured lateral images of fluorescence intensity). In contrast to moesin, β1 integrins and other membrane proteins such as HLA class I were detected at the basal membrane during early spreading (Fig. 4E; and data not shown). By contrast, ezrin maintained a global peripheral distribution with some enrichment in blebs, and was less accumulated at the apical cap (Fig. 4B; supplementary material Fig. S2D,E). Therefore, both moesin and Lifeact dynamics revealed a symmetry-breaking phenomenon in the round cortex of suspended cells that generated two cortical domains; the pre-existing round cortex that is rich in moesin, and a new domain, devoid of moesin, attached to the substratum.

Importantly, cortical actin polarization was also detected in initially attached melanoma cells collected from patient-derived metastatic fluids (pleural effusion) as well as in resting circulating lymphocytes directly isolated from blood (supplementary material Fig. S2F,G), suggesting that this mechanism of initial cortical polarity of fluid-borne cells might be operative in primary cells.

Functional regulation of moesin

C-terminal phosphorylation of a conserved threonine (T567 ezrin, T564 radixin and T558 moesin) fully activates ERM proteins at the membrane and exposes the actin-binding domain (Matsui et al., 1998). Various kinases, including protein kinase C (PKC) and Rho kinase (ROCK), phosphorylate this regulatory threonine, which is in turn dephosphorylated by calyculin-sensitive phosphatases (Ivetic and Ridley, 2004). To explore the mechanism(s) that control moesin during spreading, we used western blot to analyze global levels of phosphorylated ERM (ERM-*P*) (Fig. 5A,B). BLM cells showed the highest levels of moesin-*P* and ezrin-*P* immediately after detachment, followed by downregulation after 60 minutes in suspension due to activation of calyculin-A-sensitive Ser/Thr phosphatases (Fig. 5A; and data not shown). Interestingly, a peak of ERM phosphorylation was consistently detected following re-plating after 60 minutes in suspension, and a steady reduction was observed during the spreading process. In parallel samples, we analyzed the Ser19 phosphorylation of the myosin light chain (MLC-*P*), which is indicative of actomyosin contractility. Similar kinetics of MLC dephosphorylation in suspension followed by adhesion-induced phosphorylation were detected (Fig. 5A).

To test the pathways leading to adhesion-dependent ERM phosphorylation, we used acute treatments with inhibitors of Ser/Thr phosphatases (calyculin A) and kinases (Y-27632 and Ro-31-8220) throughout the spreading process. The distinct effect of kinase inhibitors at specific time-points during spreading revealed the contribution of both PKC and ROCK to the initial adhesion-dependent activation of ERMs, whereas the response to calyculin during the spreading process indicated the progressive activation of one or more phosphatases to balance the action of the kinases (Fig. 5C). Immunofluorescence experiments showed both ERM-*P*

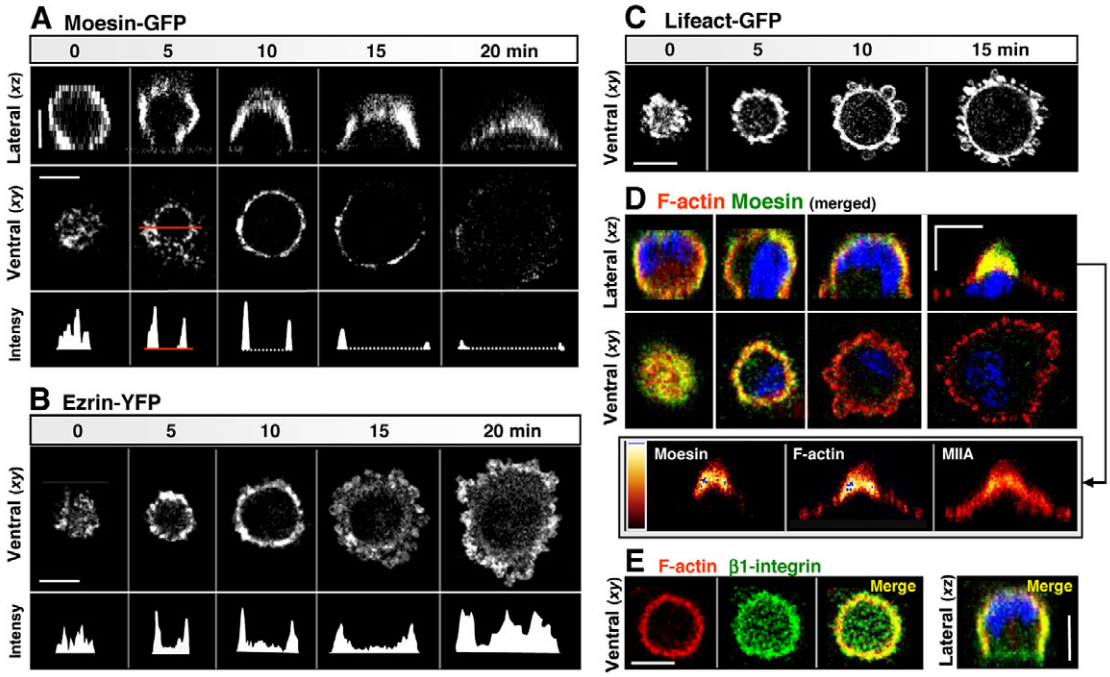

Fig. 4. Dynamic distribution of ezrin and moesin during cell spreading, (A) Cell expressing moesin-GFP live-imaged at 5 minute intervals during spreading on 2D collagen. Moesin-GFP distribution is shown in consecutive lateral views (*xz* planes) and their corresponding basal cell planes (*xy*), as indicated. Bottom panel: fluorescence intensity profiles (a.u.) measured by drawing a line (red line) at the basal cell planes and plotting the fluorescence intensity of the corresponding pixels. (B) Cell expressing ezrin-YFP live-imaged as in A. The basal planes corresponding to the ventral cell surface and the intensity profiles (a.u.) are shown. (C) Cell expressing the F-actin marker Lifeact-GFP live-imaged as in A, the basal planes are shown at the indicated times. (D) Cells at consecutive spreading phases stained for F-actin (red, phalloidin), moesin (green) and DNA (blue). Lateral (*xz*) and basal (*xy*) planes show merged images of the following phases: cell contact, cortical aperture, basal blebbing, and lamella extension/flattening-capping. The last spreading phase was analyzed in additional bottom panels that show pseudo-coloured lateral views of moesin, F-actin and myosin IIA (MIIA). Note the total, partial and slight redistribution of each protein at the apical cap. (E) Cell imaged at its basal surface during initial attachment. F-actin is in red, β1 integrin in green. Merged images are shown, including the lateral view (*xz*) and DAPI staining (blue). Scale bars: 10 μm.

and MLC-*P* staining at the unbound cortical dome of early spreading cells, and also at the apical cortex of intermediate spreading cells (Fig. 5D, left and right cells, respectively). Most ERM-*P* colocalized with moesin during spreading, but not with ezrin (supplementary material Fig. S2E). Moesin remained significantly associated with the cortex and was not observed in the cytoplasm, even after extensive treatment with kinase inhibitors (supplementary material Fig. S2H). Indeed, Hao et al. have shown that reduction of PtdIns(4,5)P_2 levels is implicated in the release of ERM proteins from lymphocyte membranes (Hao et al., 2009).

Interestingly, PtdIns(4,5)P_2 levels [visualized with the PH domain from phospholipase Cδ (PLCδ) fused to GFP] dropped at the central area of the attached membrane in phase 1 of spreading, and were significantly enhanced at the dorsal cell surface in phase 2 (supplementary material Fig. S2I). The tight coupling between moesin distribution and PtdIns(4,5)P_2 levels at the cortex during initial attachment and spreading is consistent with the current suggestion that ERM molecules target the cell membrane by binding PtdIns(4,5)P_2 (Fievet et al., 2004). In addition, the dynamic turnover of phosphorylation that couples moesin to cortical actin flow might contribute to the regulation of moesin redistribution at the cortex.

Moesin depletion or modification of its actin-binding ability impairs cell morphological transitions

Recent studies in *Drosophila* have shown that moesin plays a key role in the establishment of a stiff, rounded cortex in mitotic cells (Carreno et al., 2008; Kunda et al., 2008). Similarly, moesin-siRNA cells in suspension displayed a blebbing surface appearance and an elevated morphological complexity measured by flow cytometry (supplementary material Fig. S2J; ~1.5-fold higher side-scatter than control siRNA cells). Major changes in the initial phases of cell spreading were evident in cells with reduced moesin expression, which spread faster than control cells. These cells skipped the blebbing phase, rapidly flattened the cell body and extended a lamella (Fig. 6A), suggesting that the rounding activity of moesin delays spreading. The effect of moesin siRNA in cell spreading could be reversed by expressing a moesin-GFP cDNA that was resistant to the siRNA sequence (supplementary material Fig. S2K).

We modified the actin-binding ability of moesin by expression of a T558A mutation (A-moesin) equivalent to non-phosphorylated moesin, or a T558D mutation (D-moesin) that mimics the phosphorylated form (Huang et al., 1999). We also used an N-terminal fragment of moesin (N-moesin) that is unable to bind actin (Amieva et al., 1999). Most cells expressing inactive A-moesin, active D-moesin, or the dominant-negative N-moesin displayed a tall hemispheric cell body with a thin lamellipodium, indicating inability to flatten the cell body (Fig. 6B,C). Similarly, the three moesin mutants failed in the 'round-to-elongated transition' within the 3D matrix, remaining rounded even after 24 hours (Fig. 6D). Therefore, regulation of moesin-actin binding activity is necessary for morphological transitions to be completed.

Interestingly, a significant portion of D-mutants displayed a very active phenotype when plated on 2D or 3D collagens; periodic waves

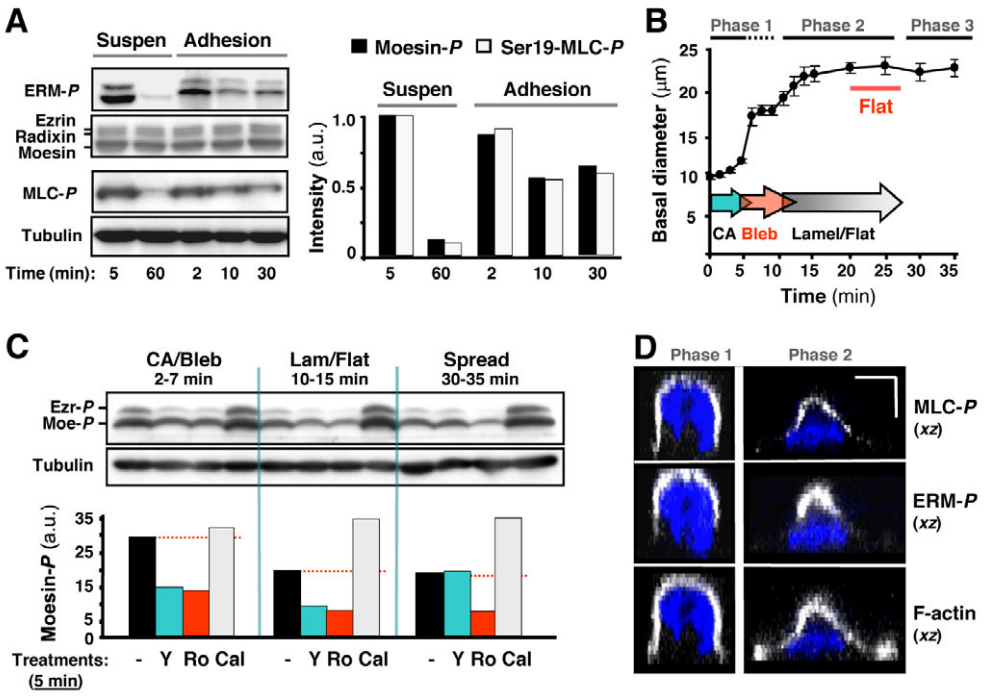

Fig. 5. ERM and MLC phosphorylation dynamics during spreading. (A) Western blot analysis of ERM-*P* and MLC-*P* levels at indicated times of suspension and spreading. BLM cells were detached and maintained in suspension for 60 minutes before re-plating on 2D collagen. Representative immunoblots show ERM-*P* and MLC-*P* levels; total ERMs and α-tubulin proteins are the respective loading controls. Densitometrical analysis shows moesin-*P* and MLC-*P* levels relative to the first time-point (5 minute suspension value set at 100%). See the spreading phases on panel B. (B) Kinetic analysis of BLM cells spreading on 2D collagen. The mean cell diameters ± s.e. are plotted at indicated times (n=6). The timing of cell spreading phases is shown. Note that the blebbing period is variable and might coincide in time with either the initial cortical aperture (CA) and/or the lamella extension (Lamel/Flat). (C) Analysis of ROCK, PKC and Ser/Thr phosphatase activities at distinct phases of spreading. Short treatments (5 minutes) with non-inhibitor, 20 μM Y-27632 (Y), 5 μM Ro-31-8820 (Ro) and 100 nM calyculin A (Cal) were individually applied to cells at 2, 10 and 30 minutes of spreading. Densitometrical analysis of moesin-*P* levels is shown in arbitrary units. The spreading phases are as shown on panel B. (D) Representative cells imaged at phase 1 or cortical aperture/blebbing (left), and phase 2 or lamella extension/flattening (right). Distribution of MLC-*P*, ERM-*P* and F-actin are shown separately at lateral *xz* planes (all in white). DAPI staining is in blue. Scale bars: 10 μm.

of cortical contractility moved throughout the cell, displacing most cytoplasm and nucleus from side to side (Fig. 6E; supplementary material Movie 2). Intriguingly, these oscillatory movements appeared to lack directionality. At the attached pole, D-moesin-expressing cells appeared to repeatedly open and close basal holes without blebbing. Fixed cells showed the nucleus passing through constrictive rings and irregularly distributed cortical actin (Fig. 6C).

Depletion of moesin impairs activation of RhoA and myosin II contractility

As reciprocal relationships between ERM proteins and Rho have been described previously (Ivetic and Ridley, 2004), we measured RhoA activity in control-, moesin- and ezrin-siRNA cells (Fig. 7A). In cells transfected with control and ezrin siRNA, RhoA activity maintained a basal level in suspended cells, and showed a triphasic response during early, intermediate and later phases of spreading (2, 10 and 60 minutes, respectively). Thus, initial contact with the substratum triggered RhoA activation, followed by a transient decrease in RhoA activity and recovery after 1 hour. Importantly, in moesin-siRNA cells, RhoA activity was barely enhanced at 2 minutes, and was completely suppressed at 10 minutes and later time-points. Consequently, moesin-depleted cells displayed a poor activation of myosin II contractility in response to initial attachment and spreading, as indicated by MLC-*P* levels (Fig. 7B). These results indicated that moesin is required to activate RhoA signalling in response to initial attachment and spreading.

Discussion

A first polarizing event of fluid-borne round cells is required during initial attachment to endothelium prior to extravasation. Our results show how moesin is important for establishment of cortical polarity following initial attachment. We used different approaches (dynamics analysis on 2D and 3D matrices, mutagenesis, RNA interference) to characterize the mechanism of moesin polarity and its role in regulating the stability of the dorsal cortex. Accordingly, we show that moesin depletion impaired the ability of melanoma cells to invade a 3D matrix, to colonize the lungs of mice, or to activate RhoA in response to adhesion.

In contrast to 2D migration, specific mechanisms control 3D invasion, which is mainly dependent on myosin II contractility and is independent of ligand density (Doyle et al., 2009; Even-Ram and Yamada, 2005). We identified moesin as a key player in 3D invasion and in adhesion-dependent activation of RhoA and subsequent myosin II contractility. ERM proteins have been reported to induce Rho activation by displacing Rho-GDI from Rho, or through their association with hamartin (Lamb et al., 2000; Takahashi et al., 1997). Moreover, ERM proteins can be activated downstream of Rho, thus potentially amplifying the Rho signal by a feedback mechanism (Shaw et al., 1998; Yonemura et al., 2002). Thus, moesin might be initially activated by a Rho-independent signal, such as integrin-mediated PKC activation (Clark and Brugge, 1995), and subsequently, a positive moesin/RhoA feedback loop could promote further Rho activation.

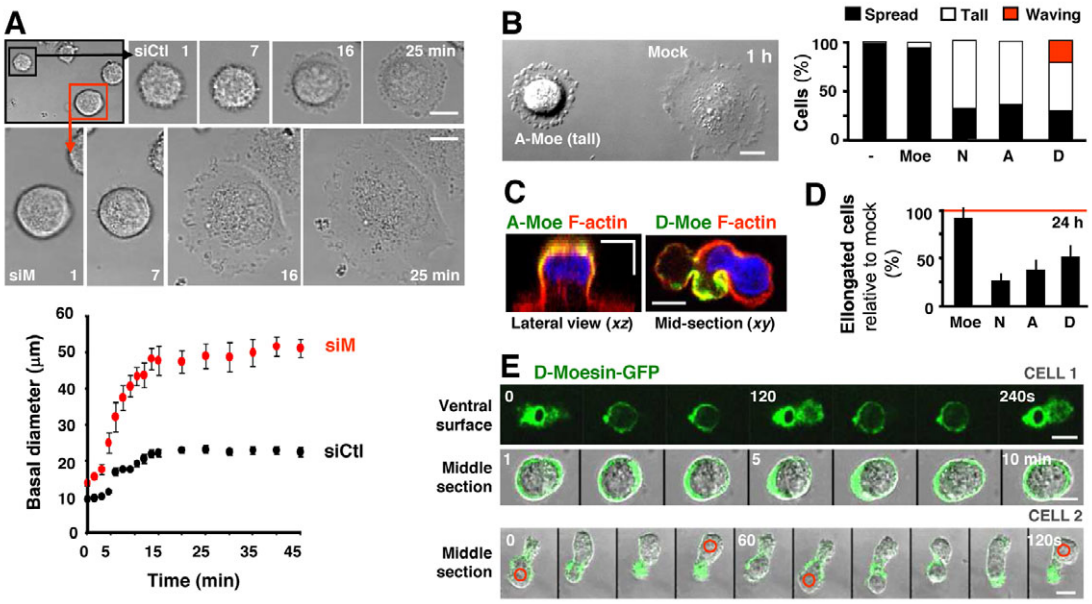

Fig. 6. Effects of moesin silencing and T558-mutation on spreading and 3D invasion. (A) BLM cells transfected with control (siCtrl) or moesin1 (siM) siRNAs live-imaged during spreading on the same collagen-coated surface (cells were differently coloured to discriminate, not shown). DIC images and the plotted cell diameters, means ± s.e. (n=4 cells by siRNA) are shown. Moesin-silenced cells completed flattening in ~5 minutes, control cells needed at least 20–25 minutes. (B) Morphological analysis of BLM cells expressing no (–), full-length (Moe) , N-, A- or D-moesin–GFP constructs after 1 hour of spreading. Histograms denote the percentage of spread/flattened, tall and waving cells (100 cells per experiment, n=3). The 'tall' phenotype corresponds to cells that have extended a lamella (≥20 µm wide) but have not flattened the cell body (≥10 µm tall). Compare A-moesin (A-Moe) cell with the mock cell in the DIC image. For 'waving' cells see E, or supplementary material Movie 2. (C) Cells expressing A- and D-moesin–GFP (green) stained with phalloidin (red) and DAPI (blue). Left: A-moesin cell displaying the 'tall' phenotype in a lateral view (*xz*). Right: D-moesin cell showing the waving phenotype and the irregular actin cortex in a middle-section. (D) Morphological analysis of BLM cells expressing full-length, N-, A- or D-moesin–GFP after 24 hours incubation on 3D collagen. The histograms denote the mean percentage ± s.e. of elongated cells relative to control mock cells (100 cells per experiment, n=3). (E) Cyclic movements of BLM cells transfected with D-moesin–GFP and live-imaged. Two different cells are shown. Cell 1 is shown at the basal and equatorial confocal planes, as indicated. Note the repetitive opening and closing at the ventral surface. Cell 2 is shown at a middle confocal plane. Note the nucleus (red circle) passing through a constrictive ring. Fluorescence is shown merged with DIC in the middle confocal plane galleries. Scale bars: 10 µm.

The spatiotemporal relationship between moesin-*P* and MLC-*P* suggests that moesin could coordinate Rho activation and myosin II contractility during early adhesion. RhoA activity at the back of a moving cell is necessary to limit protrusive activity and Rac activation to the front (Burridge and Doughman, 2006). Furthermore, limited Rac activation produces directionally persistent cell migration instead of random locomotion on 2D surfaces, and favours 3D migration (Pankov et al., 2005). Our data indicate that polarized moesin restricts instability and blebs to the attached pole, leading to directional vertical migration into 3D matrices. Indeed, knockdown of moesin produced a striking superficial spreading on the surface of 3D matrices that resembled Rho-ROCK inhibition (Wyckoff et al., 2006). Furthermore, we hypothesize that polarized moesin-Rho-myosin-II contractility at the dorsal cortex could direct hydrostatic pressure towards the invasive blebbing pole. Accordingly, the presence of polarized blebs at the invasive pole or around early spreading cells is a sign of hydrostatic pressure generated by actomyosin contractility (Charras et al., 2008).

It is worth emphasizing that although moesin expression is necessary for invasion, regulated removal from the attached pole is required to allow transition from stationary round cells to more flexible migration-related morphologies. It has been reported that PtdIns(4,5)P_2 hydrolysis might release ERM from membranes and activate cofilin, which binds to and severs F-actin (Hao et al., 2009; van Rheenen et al., 2007). Thus, integrin-mediated depletion of PtdIns(4,5)P_2 might facilitate initial disruption of the stable cortex of round cells (Clark and Brugge, 1995). Importantly, moesin-GFP and Lifeact-GFP dynamics revealed for the first time a cortical symmetry-breaking event during early attachment of tumour cells to both 2D and 3D matrices. This is a common mechanism for creating cortical polarity in non-adherent single-cell embryos; local disruption of a contractile cortex provokes the remaining network to contract away, triggering a symmetry-breaking phenomenon that establishes contractile and non-contractile cortical regions (Cowan and Hyman, 2007; Paluch et al., 2006). Similarly, the polarizing response of the contractile cortex of round cells generates two domains: a moesin-rich dorsal cortex and a moesin-free membrane domain with polarized blebs (see our model in Fig. 8). This polarized blebbing cell initiates 3D invasion, but a cell cannot move vertically on 2D surfaces and, after a transitory blebbing period, switch to the second phase of spreading that is characterized by rapid lamella extension and capping. Once moesin polarity is initiated, additional mechanism(s) help to maintain moesin exclusion from the invasive pole, as indicated by moesin mutants that produced round cells being unable to adopt a mesenchymal morphology within 3D matrices, or to fully spread on 2D surfaces.

The phenotype of the phosphomimetic mutant, which appeared to open and close basal holes, and displayed curious oscillating behaviours, was reminiscent of the oscillatory phenomenon produced by recurrent cortical ruptures followed by re-formation of the broken cortex, suggesting that this mutant repeatedly reassembled round cell cortices (Paluch et al., 2006). Therefore, inactivation of the rounding activity of moesin-*P* might be required to maintain a stable invasive pole. Both A- and N-moesin mutants

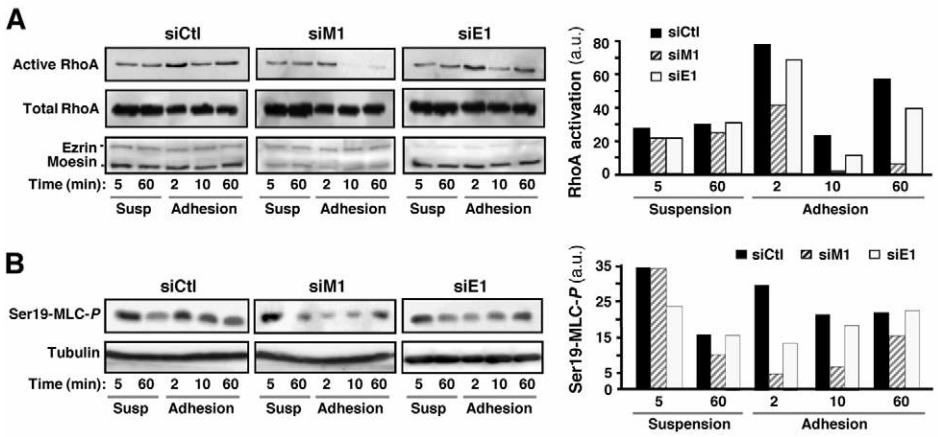

Fig. 7. Effects of moesin and ezrin silencing on adhesion-dependent RhoA activation and on MLC phosphorylation. (A) Analysis of RhoA activation in BLM cells transfected with control, meosin1 (siM1) or ezrin1 (siE1) siRNA. Cells were assessed at the indicated times of suspension and spreading on 2D collagen. Representative immunoblots show active-RhoA, total-RhoA, and moesin and ezrin expression. Densitometrical analysis for active GTP-RhoA is shown. (B) Ser19-MLC phosphorylation was analyzed as in A. Representative immunoblots show MLC-*P*, and α-tubulin as loading control. Densitometrical analysis for MLC-*P* is shown.

bind to the membrane by targeting PtdIns(4,5)P_2 but are unable to bind actin. Consequently, these mutants are unable to regulate receptor distribution and signalling at the cortex during the cortical flow phase 2 of spreading, producing a 'tall' spreading. Indeed, the rounding activity of moesin delays the process of spreading and, thereby, moesin-depleted cells become flat more easily. Together, these data suggest that a cortical symmetry-breaking event initiates moesin polarity, which is further consolidated by local inactivation of its phosphorylation state at the attached/invasive pole.

Moesin, the only member of the ERM family expressed in *Drosophila*, has been shown to play a crucial role in the generation of a rigid and uniform cell cortex during mitosis and in the establishment of embryo polarity (Carreno et al., 2008; Jankovics et al., 2002; Kunda et al., 2008; Polesello et al., 2002). We show that moesin participates in the regulation of the round cortex and in the establishment of polarity, thus suggesting that mammalian moesin is functionally equivalent to *Drosophila* moesin. However, genetic results in Drosophila suggest that moesin functions antagonistically to Rho pathway activity (Speck et al., 2003). This is in contrast to most studies performed in mammalian cells that indicate that ERM proteins positively regulate Rho activity (Bretscher et al., 2002). Our work indicates that the relationship between ERM proteins and Rho pathway appears to be cell-context-dependent and more complex than initially suspected. ERM proteins are generally believed to be functionally redundant, and most works only analyze one member of the ERM family (Hughes and Fehon, 2007). Interestingly, distinct ezrin and moesin distributions were recently reported in lymphocytes (Ilani et al., 2007). In addition to different distribution, we found opposite roles for ezrin and moesin depletion in 3D collagen invasion. Accordingly, only moesin depletion impaired adhesion-dependent Rho and subsequent myosin II activation in melanoma cells. Consistent with our results, specific depletion of ezrin enhanced 3D matrix invasion of colon carcinoma cells (Hiscox and Jiang, 1999). In fact, it has been reported that ezrin expression promotes an early survival advantage for metastatic cells, although its role in invasion was not addressed (Khanna et al., 2004). Our working hypothesis is that moesin conserves a major role in organizing the stable cortex of round cells and the rear pole of moving cells, whereas ezrin participates in organizing more dynamic actin structures, such as blebs, filopodia or lamellipodia at the leading edge. In line with this proposal, moesin forms the cortices of round leukocytes and is generally accumulated at their back during migration (Serrador et al., 1997), whereas ezrin promotes leading-edge protrusions through Dbl recruitment and Cdc42 activation (Prag et al., 2007).

Our results highlight the importance of the thick round cortex of circulating cells in driving the extravasation step of the metastatic process. We propose that moesin plays a specific role in orienting a contractile cortical response that powers fluid-to-solid tissue transition of tumour cells. Consequently, this mechanism of moesin polarity might sustain extravasation of circulating cells during metastasis.

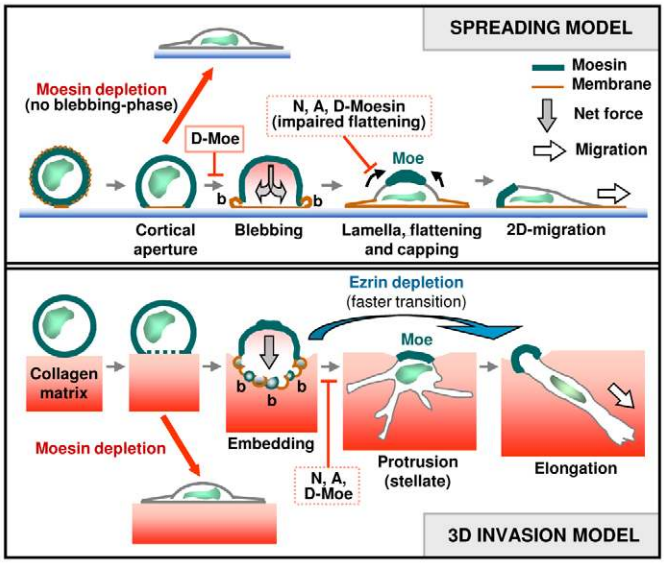

Fig. 8. 2D spreading and 3D invasion models. Schematic representation of 2D spreading and 3D invasion. On the basis of the tight spatio-temporal control of moesin and actomyosin cortical dynamics, we depict sequential phases of the fluid-to-solid cell transition. Originally, unattached fluid-phase cells are rounded and symmetric, and display a continuous cortical distribution of moesin. Upon early attachment, both on 2D and 3D collagen, a cortical symmetry-breaking event generates two domains: a moesin-rich dorsal dome and a moesin-free attached/invasive domain. At this rounded asymmetric state, cells show peripheral blebs (b) on 2D, or invasive multiple blebs on 3D, indicating cortical contractility and hydrostatic pressure. At this point, moesin stabilizes the contractile actomyosin cortex and directs the net force vector towards the attached pole. On 2D coated surfaces, the stabilizing function of moesin delays spreading and causes a transient blebbing phase. Flattening of the round cell body requires moesin downregulation and removal from the attached cell pole towards an apical cap. By contrast, on 3D collagen, moesin provides cortical actin stability and sustains activation of Rho, ROCK and myosin contractility at the dorsal dome, which leads to cytoplasmic streaming to invade the matrix, as in amoeboid movement. After embedding, cells extend multiple protrusions and/or elongate. The inhibitory effects of moesin mutants and the phenotypes observed for moesin- and ezrin-silenced cells are indicated.

Materials and Methods

Cells

The highly invasive melanoma cell lines BLM, MV3 (both provided by Goos Van Muijen, Radboud University, Nijmegen, The Netherlands) and Skmel-103, Skmel-147 and Skmel-19 from Maria S. Soengas (Centro Nacional de Investigaciones Oncológicas, Madrid) were used in this study, as well as the A375 and MeWo melanoma cell lines (ATCC). Cells were maintained in Roswell Park Memorial Institute (RPMI)-1640 medium or Dulbecco's modified Eagle's medium (DMEM) (Gibco) supplemented with 10% fetal calf serum (FCS) (Harlam Sera-lab), detached with EDTA, and starved in suspension for ~1 hour before use in assays. Primary human umbilical vein endothelial cells (HUVEC) were obtained from umbilical cords and grown as previously described (Longo et al., 2001).

Antibodies, dyes and inhibitors

Anti-moesin 38/87 and EP1863Y (Abcam), ERM-*P* and Ser19-*P*–myosin light chain 2 (Cell Signaling), ezrin sc-32759 and RhoA sc-418 (Santa Cruz Biotechnology), and myosin heavy chain IIA and α-smooth muscle actin (Sigma), were used as primary antibodies. Anti-HLA I (W6/32), β1 integrin (TS2/16), and blocking β1 integrin (Lia1/2) Abs were provided by Francisco Sánchez-Madrid (Hospital de la Princesa, Madrid, Spain). Secondary Abs conjugated to FITC, Cy3, Texas red and Cy5 were purchased from Jackson ImmunoResearch. Calcein, Orange-CMTMR and FITC- or Texas-red-conjugated phalloidin specific for F-actin were obtained from Molecular Probes; propidium iodide and DAPI were from Sigma. ROCK inhibitor Y-27632 (Sigma), metalloproteinase inhibitor GM6001 (Calbiochem), Ser/Thr phosphatase inhibitor calyculin A (Calbiochem), and PKC inhibitor Ro-31-8220 (Calbiochem) were used.

Fluorescent proteins and siRNAs

Moesin tagged to GFP, or ezrin tagged to YFP in the C-terminus were used to study the dynamic distribution of these proteins. Most available data, including moesin-GFP expression in living organisms (Edwards et al., 1997), indicate that this tag does not interfere with the conformational regulation of ERM proteins. Only cells with a moderate level of expression of moesin-GFP were used in experiments, and they behaved similarly to the untransfected cells. Moesin-GFP distribution was similar to that of the endogenous protein. Moesin-GFP and N-terminal fragment (residues 1-310) of moesin-GFP were provided by Francisco Sánchez-Madrid, and ezrin-YFP by Miguel A. Quintanilla (Instituto de Investigaciones Biomédicas, Madrid, Spain). T558-moesin mutants were generated using the QuikChange II Site-Directed Mutagenesis Kit. The PH-GFP domain of PLCδ protein was provided by Mario Rebecchi (St. John's University, NY), and the F-actin marker Lifeact-GFP by Roland Wedlich-Soldner (Max-Planck Institute, Martinsried, Germany).

The siRNA sequences of moesin1 (5′-AGAUCGAGGAACAGACUAA-3′), ezrin1 (5′-UCCACUAUGUGGAUAAUAA-3′) and ezrin2 (5′-AAGGAAUCCUUAG-CGAUGA-3′) were provided by F. Sánchez-Madrid (Barrero-Villar et al., 2009). Moesin2 (sc-35955) and control (sc-37007) siRNAs were purchased from Santa Cruz Biotechnology. Both GFP-constructs and siRNAs were transfected with Lipofectamine 2000 according to the manufacturer's instructions (Invitrogen). Cells were used ~24 hours after DNA transfection, and the relative expression of the different mutants assessed by flow cytometry, showing that they were comparable. For silencing, cells were transfected for 2 consecutive days with 33 nM siRNA, and used ~24 hours after the second transfection. Interference efficiency was evaluated by western blot. All the results obtained with moesin1 and ezrin1 siRNAs were reproduced by the second pair of siRNAs moesin2 and ezrin2 (usually not shown to avoid redundant information).

3D collagen and endothelial invasion assays

For quantitative 3D-invasion assays, thick collagen gels of ~500 μm in depth were prepared by incubating 50 μl of 2.4 mg/ml type I collagen (Inamed Biomaterials) in medium-199 (Gibco) for 1 hour at 37°C in 8-μm pore Transwell chambers (Costar, Corning, NY). 10^4 cells suspended in 0.4% BSA/RPMI-1640 were plated on gels and allowed to invade for 24 or 48 hours. Cells were then fixed with 4% formaldehyde and stained with propidium iodide. To promote chemotaxis, the lower chamber was filled with 10% FCS/RPMI-1640. For quantification, confocal *z*-stacks were acquired at 10-μm intervals from the gel surface using a 10× PL-APO NA 0.4 objective; cells were considered invasive beyond a 20-μm depth. Comparative analyses were performed with distinct siRNA-transfected melanoma cell lines, and with BLM cells blocked with Abs or treated with different doses of Y-27632 (pre-treated for 1 hour) or GM6001 (pre-treated overnight in serum-free medium).

For qualitative morphological analyses, thick collagen matrices (~300 μm) were similarly polymerized in multi-well slides (IBIDI). Transfected BLM cells were allowed to invade for 2 and 24 hours before staining with phalloidin-FITC. Imaging was performed with a 10× lens or a 20× PL-APO NA 0.7 glycerol immersion objective. To acquire higher resolution images, cells were plated on thin collagen matrices (<100 μm) directly polymerized on coverslips, and imaged with a 63× PL-APO NA 1.3 immersion objective (Fig. 3D,E).

Imaging of trans-endothelial migration was performed through HUVEC monolayers grown on thick collagen gels for at least 24 hours. BLM cells were then placed on the confluent endothelium and live-imaged during invasion. After 24 hours, the samples were fixed for quantification. Parallel silver-staining at distinct states of the process was performed to visualize endothelial junctions, as previously described (Longo et al., 2001). For higher resolution imaging (63× lens), HUVEC monolayers were grown on thin collagen gels (<100 μm) (Fig. 3B).

Spreading and GTPase analyses

For spreading analysis, cells were detached and maintained in suspension at 37°C for 1 hour in 0.4% BSA/RPMI-1640, plated on coverslips coated with 5 μg/ml collagen I (2D collagen) and incubated at 37°C for different times. Cells in suspension or at specific phases of spreading were fixed, stained and imaged by confocal microscopy, or directly lysed in Laemmli sample buffer for immunoblot analysis.

For GTPase assays, BLM cells were resuspended in 0.5% BSA/DMEM, incubated in suspension at 37°C, or added to plates coated with 5 μg/ml collagen I for different time periods. Cells were then detached and lysed. Aliquots from extracts were kept for total lysate controls, whereas the remaining volume was mixed with glutathione *S*-transferase (GST)-C21 fusion protein in the presence of glutathione-agarose beads. Following incubation, bound proteins were eluted in Laemmli buffer and analyzed by western blot using an anti-RhoA antibody, as previously described (Bartolome et al., 2004).

Fluorescence confocal microscopy

A confocal scanning inverted Leica AOBS/SP2-microscope (Leica Microsystems) provided with controlled CO_2 and temperature stage was used for time-lapse and static imaging. For indirect immunofluorescence, cells were fixed with 4% formaldehyde and permeabilized with 0.5% Triton X-100, and labelled with the corresponding Abs. Incubation times were longer for cells invading collagen matrices, which were directly imaged without mounting. BLM cells were live-imaged in controlled stages at 37°C and in 5% CO_2. For time-lapse *z*-sectioning, the minimum number of series and sections were acquired to reduce photobleaching and phototoxicity as much as possible (Figs 3 and 4). Cells imaged at the cortical aperture or during the flattening/capping phases of spreading, and cells invading 3D collagen gels often needed to be shown as lateral views, corresponding to single *xz* or *yz* planes, or to 3D-reconstructions (maximum projections along the *y*-axis). These images were processed from serial *z*-stacks acquired at ~0.3-μm intervals, with the *z*-axis limits ~1 μm beyond the cell confines for optimal visualization of cortical holes or apical caps. Calcein staining and protein caps sometimes appear intentionally saturated, and therefore size-overestimated, in order to detect narrow invasive protrusions or alternative minor distributions, respectively. Collagen fibres were detected by light reflection throughout the study, thus enabling us to determine the gel surface position (depicted on lateral views as horizontal lines). Image processing and measurements were assessed using Leica Confocal Software LCS-15.37.

Lung colonization assays

For the in vivo lung assays, BLM cells transfected with siCtl and siMoe or siEzr were loaded with Orange-CMTMR and calcein cell trackers, respectively, mixed in equal proportion (10^6 cells by siRNA), and injected into the tail vein of mice, as previously described (Pinner and Sahai, 2008). At 20 minutes or 20 hours after injection, lungs were extracted, fixed in formaldehyde, and directly imaged with a 10× objective. Over 150 colonizing cells from >30 fields were counted at 20 hours.

We thank Francisco Sánchez-Madrid, Goos Van Muijen, Maria S. Soengas, Miguel A. Quintanilla, Roland Wedlich-Soldner and Mario Rebecchi for kindly providing cells and reagents, and Balbino Alarcón for helpful comments on the manuscript. We are grateful to Alexandra de Francisco for mice handling, Julia Villarejo and Isabel Treviño for expert technical assistance, and members of the Hospital Gregorio Marañón Obstetrics Service for providing the umbilical cords. This work was supported by grants awarded to P.S.-M. from the Spanish Ministry of Education and Science (SAF-2006-08615) and Fundación Ramón Areces.

References

Amieva, M. R., Litman, P., Huang, L., Ichimaru, E. and Furthmayr, H. (1999). Disruption of dynamic cell surface architecture of NIH3T3 fibroblasts by the N-terminal domains of moesin and ezrin: in vivo imaging with GFP fusion proteins. *J. Cell Sci.* **112**, 111-125.

Barrero-Villar, M., Cabrero, J. R., Gordon-Alonso, M., Barroso-Gonzalez, J., Alvarez-Losada, S., Munoz-Fernandez, M. A., Sanchez-Madrid, F. and Valenzuela-Fernandez, A. (2009). Moesin is required for HIV-1-induced CD4-CXCR4 interaction, F-actin redistribution, membrane fusion and viral infection in lymphocytes. *J. Cell Sci.* **122**, 103-113.

Bartolome, R. A., Galvez, B. G., Longo, N., Baleux, F., Van Muijen, G. N., Sanchez-Mateos, P., Arroyo, A. G. and Teixido, J. (2004). Stromal cell-derived factor-1alpha promotes melanoma cell invasion across basement membranes involving stimulation of membrane-type 1 matrix metalloproteinase and Rho GTPase activities. *Cancer Res.* **64**, 2534-2543.

Bornens, M., Paintrand, M. and Celati, C. (1989). The cortical microfilament system of lymphoblasts displays a periodic oscillatory activity in the absence of microtubules: implications for cell polarity. *J. Cell Biol.* **109**, 1071-1083.

Bretscher, A., Edwards, K. and Fehon, R. G. (2002). ERM proteins and merlin: integrators at the cell cortex. *Nat. Rev. Mol. Cell Biol.* **3**, 586-599.

Brown, M. J., Nijhara, R., Hallam, J. A., Gignac, M., Yamada, K. M., Erlandsen, S. L., Delon, J., Kruhlak, M. and Shaw, S. (2003). Chemokine stimulation of human peripheral blood T lymphocytes induces rapid dephosphorylation of ERM proteins, which facilitates loss of microvilli and polarization. *Blood* **102**, 3890-3899.

Burridge, K. and Doughman, R. (2006). Front and back by Rho and Rac. *Nat. Cell Biol.* **8**, 781-782.

Carreno, S., Kouranti, I., Glusman, E. S., Fuller, M. T., Echard, A. and Payre, F. (2008). Moesin and its activating kinase Slik are required for cortical stability and microtubule organization in mitotic cells. *J. Cell Biol.* **180**, 739-746.

Chambers, A. F., Groom, A. C. and MacDonald, I. C. (2002). Dissemination and growth of cancer cells in metastatic sites. *Nat. Rev. Cancer* **2**, 563-572.

Charafe-Jauffret, E., Monville, F., Bertucci, F., Esterni, B., Ginestier, C., Finetti, P., Cervera, N., Geneix, J., Hassanein, M., Rabayrol, L. et al. (2007). Moesin expression is a marker of basal breast carcinomas. *Int. J. Cancer* **121**, 1779-1785.

Charras, G. T., Coughlin, M., Mitchison, T. J. and Mahadevan, L. (2008). Life and times of a cellular bleb. *Biophys. J.* **94**, 1836-1853.

Clark, E. A. and Brugge, J. S. (1995). Integrins and signal transduction pathways: the road taken. *Science* **268**, 233-239.

Condeelis, J., Singer, R. H. and Segall, J. E. (2005). The great escape: when cancer cells hijack the genes for chemotaxis and motility. *Annu. Rev. Cell Dev. Biol.* **21**, 695-718.

Cowan, C. R. and Hyman, A. A. (2007). Acto-myosin reorganization and PAR polarity in C. elegans. *Development* **134**, 1035-1043.

Doyle, A. D., Wang, F. W., Matsumoto, K. and Yamada, K. M. (2009). One-dimensional topography underlies three-dimensional fibrillar cell migration. *J. Cell Biol.* **184**, 481-490.

Edwards, K. A., Demsky, M., Montague, R. A., Weymouth, N. and Kiehart, D. P. (1997). GFP-moesin illuminates actin cytoskeleton dynamics in living tissue and demonstrates cell shape changes during morphogenesis in Drosophila. *Dev. Biol.* **191**, 103-117.

Even-Ram, S. and Yamada, K. M. (2005). Cell migration in 3D matrix. *Curr. Opin. Cell Biol.* **17**, 524-532.

Faure, S., Salazar-Fontana, L. I., Semichon, M., Tybulewicz, V. L., Bismuth, G., Trautmann, A., Germain, R. N. and Delon, J. (2004). ERM proteins regulate cytoskeleton relaxation promoting T cell-APC conjugation. *Nat. Immunol.* **5**, 272-279.

Fievet, B. T., Gautreau, A., Roy, C., Del Maestro, L., Mangeat, P., Louvard, D. and Arpin, M. (2004). Phosphoinositide binding and phosphorylation act sequentially in the activation mechanism of ezrin. *J. Cell Biol.* **164**, 653-659.

Giannone, G., Dubin-Thaler, B. J., Dobereiner, H. G., Kieffer, N., Bresnick, A. R. and Sheetz, M. P. (2004). Periodic lamellipodial contractions correlate with rearward actin waves. *Cell* **116**, 431-443.

Hao, J. J., Liu, Y., Kruhlak, M., Debell, K. E., Rellahan, B. L. and Shaw, S. (2009). Phospholipase C-mediated hydrolysis of PIP2 releases ERM proteins from lymphocyte membrane. *J. Cell Biol.* **184**, 451-462.

Hiscox, S. and Jiang, W. G. (1999). Ezrin regulates cell-cell and cell-matrix adhesion, a possible role with E-cadherin/beta-catenin. *J. Cell Sci.* **112**, 3081-3090.

Huang, L., Wong, T. Y., Lin, R. C. and Furthmayr, H. (1999). Replacement of threonine 558, a critical site of phosphorylation of moesin in vivo, with aspartate activates F-actin binding of moesin. Regulation by conformational change. *J. Biol. Chem.* **274**, 12803-12810.

Hughes, S. C. and Fehon, R. G. (2007). Understanding ERM proteins-the awesome power of genetics finally brought to bear. *Curr. Opin. Cell Biol.* **19**, 51-56.

Ilani, T., Khanna, C., Zhou, M., Veenstra, T. D. and Bretscher, A. (2007). Immune synapse formation requires ZAP-70 recruitment by ezrin and CD43 removal by moesin. *J. Cell Biol.* **179**, 733-746.

Ivetic, A. and Ridley, A. J. (2004). Ezrin/radixin/moesin proteins and Rho GTPase signalling in leucocytes. *Immunology* **112**, 165-176.

Jankovics, F., Sinka, R., Lukacsovich, T. and Erdelyi, M. (2002). MOESIN crosslinks actin and cell membrane in Drosophila oocytes and is required for OSKAR anchoring. *Curr. Biol.* **12**, 2060-2065.

Khanna, C., Wan, X., Bose, S., Cassaday, R., Olomu, O., Mendoza, A., Yeung, C., Gorlick, R., Hewitt, S. M. and Helman, L. J. (2004). The membrane-cytoskeleton linker ezrin is necessary for osteosarcoma metastasis. *Nat. Med.* **10**, 182-186.

Kobayashi, H., Sagara, J., Kurita, H., Morifuji, M., Ohishi, M., Kurashina, K. and Taniguchi, S. (2004). Clinical significance of cellular distribution of moesin in patients with oral squamous cell carcinoma. *Clin. Cancer Res.* **10**, 572-580.

Kunda, P., Pelling, A. E., Liu, T. and Baum, B. (2008). Moesin controls cortical rigidity, cell rounding, and spindle morphogenesis during mitosis. *Curr. Biol.* **18**, 91-101.

Lamb, R. F., Roy, C., Diefenbach, T. J., Vinters, H. V., Johnson, M. W., Jay, D. G. and Hall, A. (2000). The TSC1 tumour suppressor hamartin regulates cell adhesion through ERM proteins and the GTPase Rho. *Nat. Cell Biol.* **2**, 281-287.

Longo, N., Yanez-Mo, M., Mittelbrunn, M., de la Rosa, G., Munoz, M. L., Sanchez-Madrid, F. and Sanchez-Mateos, P. (2001). Regulatory role of tetraspanin CD9 in tumor-endothelial cell interaction during transendothelial invasion of melanoma cells. *Blood* **98**, 3717-3726.

Matsui, T., Maeda, M., Doi, Y., Yonemura, S., Amano, M., Kaibuchi, K. and Tsukita, S. (1998). Rho-kinase phosphorylates COOH-terminal threonines of ezrin/radixin/moesin (ERM) proteins and regulates their head-to-tail association. *J. Cell Biol.* **140**, 647-657.

Matsui, T., Yonemura, S. and Tsukita, S. (1999). Activation of ERM proteins in vivo by Rho involves phosphatidyl-inositol 4-phosphate 5-kinase and not ROCK kinases. *Curr. Biol.* **9**, 1259-1262.

Niggli, V. and Rossy, J. (2008). Ezrin/radixin/moesin: versatile controllers of signaling molecules and of the cortical cytoskeleton. *Int. J. Biochem. Cell Biol.* **40**, 344-349.

Niggli, V., Andreoli, C., Roy, C. and Mangeat, P. (1995). Identification of a phosphatidylinositol-4,5-bisphosphate-binding domain in the N-terminal region of ezrin. *FEBS Lett.* **376**, 172-176.

Paluch, E., van der Gucht, J. and Sykes, C. (2006). Cracking up: symmetry breaking in cellular systems. *J. Cell Biol.* **175**, 687-692.

Pankov, R., Endo, Y., Even-Ram, S., Araki, M., Clark, K., Cukierman, E., Matsumoto, K. and Yamada, K. M. (2005). A Rac switch regulates random versus directionally persistent cell migration. *J. Cell Biol.* **170**, 793-802.

Partridge, M. A. and Marcantonio, E. E. (2006). Initiation of attachment and generation of mature focal adhesions by integrin-containing filopodia in cell spreading. *Mol. Biol. Cell* **17**, 4237-4248.

Pinner, S. and Sahai, E. (2008). PDK1 regulates cancer cell motility by antagonising inhibition of ROCK1 by RhoE. *Nat. Cell Biol.* **10**, 127-137.

Polesello, C., Delon, I., Valenti, P., Ferrer, P. and Payre, F. (2002). Dmoesin controls actin-based cell shape and polarity during Drosophila melanogaster oogenesis. *Nat. Cell Biol.* **4**, 782-789.

Prag, S., Parsons, M., Keppler, M. D., Ameer-Beg, S. M., Barber, P., Hunt, J., Beavil, A. J., Calvert, R., Arpin, M., Vojnovic, B. et al. (2007). Activated ezrin promotes cell migration through recruitment of the GEF Dbl to lipid rafts and preferential downstream activation of Cdc42. *Mol. Biol. Cell* **18**, 2935-2948.

Riedl, J., Crevenna, A. H., Kessenbrock, K., Yu, J. H., Neukirchen, D., Bista, M., Bradke, F., Jenne, D., Holak, T. A., Werb, Z. et al. (2008). Lifeact: a versatile marker to visualize F-actin. *Nat. Methods* **5**, 605-607.

Rodriguez, O. C., Schaefer, A. W., Mandato, C. A., Forscher, P., Bement, W. M. and Waterman-Storer, C. M. (2003). Conserved microtubule-actin interactions in cell movement and morphogenesis. *Nat. Cell Biol.* **5**, 599-609.

Sahai, E. (2007). Illuminating the metastatic process. *Nat. Rev. Cancer* **7**, 737-749.

Serrador, J. M., Alonso-Lebrero, J. L., del Pozo, M. A., Furthmayr, H., Schwartz-Albiez, R., Calvo, J., Lozano, F. and Sanchez-Madrid, F. (1997). Moesin interacts with the cytoplasmic region of intercellular adhesion molecule-3 and is redistributed to the uropod of T lymphocytes during cell polarization. *J. Cell Biol.* **138**, 1409-1423.

Shaw, R. J., Henry, M., Solomon, F. and Jacks, T. (1998). RhoA-dependent phosphorylation and relocalization of ERM proteins into apical membrane/actin protrusions in fibroblasts. *Mol. Biol. Cell* **9**, 403-419.

Speck, O., Hughes, S. C., Noren, N. K., Kulikauskas, R. M. and Fehon, R. G. (2003). Moesin functions antagonistically to the Rho pathway to maintain epithelial integrity. *Nature* **421**, 83-87.

Takahashi, K., Sasaki, T., Mammoto, A., Takaishi, K., Kameyama, T., Tsukita, S. and Takai, Y. (1997). Direct interaction of the Rho GDP dissociation inhibitor with ezrin/radixin/moesin initiates the activation of the Rho small G protein. *J. Biol. Chem.* **272**, 23371-23375.

Tsuji, K., Yamauchi, K., Yang, M., Jiang, P., Bouvet, M., Endo, H., Kanai, Y., Yamashita, K., Moossa, A. R. and Hoffman, R. M. (2006). Dual-color imaging of nuclear-cytoplasmic dynamics, viability, and proliferation of cancer cells in the portal vein area. *Cancer Res.* **66**, 303-306.

Van Muijen, G. N., Cornelissen, L. M., Jansen, C. F., Figdor, C. G., Johnson, J. P., Brocker, E. B. and Ruiter, D. J. (1991). Antigen expression of metastasizing and non-metastasizing human melanoma cells xenografted into nude mice. *Clin. Exp. Metastasis* **9**, 259-272.

van Rheenen, J., Song, X., van Roosmalen, W., Cammer, M., Chen, X., Desmarais, V., Yip, S. C., Backer, J. M., Eddy, R. J. and Condeelis, J. S. (2007). EGF-induced PIP2 hydrolysis releases and activates cofilin locally in carcinoma cells. *J. Cell Biol.* **179**, 1247-1259.

Wyckoff, J. B., Pinner, S. E., Gschmeissner, S., Condeelis, J. S. and Sahai, E. (2006). ROCK- and myosin-dependent matrix deformation enables protease-independent tumor-cell invasion in vivo. *Curr. Biol.* **16**, 1515-1523.

Yonemura, S., Matsui, T. and Tsukita, S. (2002). Rho-dependent and -independent activation mechanisms of ezrin/radixin/moesin proteins: an essential role for polyphosphoinositides in vivo. *J. Cell Sci.* **115**, 2569-2580.

Yu, Y., Khan, J., Khanna, C., Helman, L., Meltzer, P. S. and Merlino, G. (2004). Expression profiling identifies the cytoskeletal organizer ezrin and the developmental homeoprotein Six-1 as key metastatic regulators. *Nat. Med.* **10**, 175-181.